

See discussions, stats, and author profiles for this publication at: <https://www.researchgate.net/publication/309491137>

Self-attraction into spinning eigenstates of a mobile wave source by its emission back-reaction

Article in *Physical Review E* · October 2016

DOI: 10.1103/PhysRevE.94.042224

CITATION

1

READS

71

4 authors, including:



Matthieu Labousse

University of Leiden

14 PUBLICATIONS 65 CITATIONS

[SEE PROFILE](#)



Stéphane Perrard

University of Chicago

14 PUBLICATIONS 89 CITATIONS

[SEE PROFILE](#)



Emmanuel Fort

École Supérieure de Physique et de Chimie In...

99 PUBLICATIONS 1,722 CITATIONS

[SEE PROFILE](#)

All content following this page was uploaded by **Emmanuel Fort** on 31 October 2016.

The user has requested enhancement of the downloaded file. All in-text references [underlined in blue](#) are added to the original document and are linked to publications on ResearchGate, letting you access and read them immediately.

Self-attraction into spinning eigenstates of a mobile wave source by its emission back-reaction

Matthieu Labousse,^{1,2,*} Stéphane Perrard,² Yves Couder,² and Emmanuel Fort^{1,†}

¹*Institut Langevin, ESPCI Paris, PSL Research University, CNRS, 1 rue Jussieu, 75005 Paris, France*

²*Matériau et Systèmes Complexes, Université Paris Diderot, CNRS, Sorbonne Paris Cité, Bâtiment Condorcet, 10 rue Alice Domon et Léonie Duquet, 75013 Paris, France*

(Received 1 June 2016; published 27 October 2016)

The back-reaction of a radiated wave on the emitting source is a general problem. In the most general case, back-reaction on moving wave sources depends on their whole history. Here we study a model system in which a pointlike source is piloted by its own memory-endowed wave field. Such a situation is implemented experimentally using a self-propelled droplet bouncing on a vertically vibrated liquid bath and driven by the waves it generates along its trajectory. The droplet and its associated wave field form an entity having an intrinsic dual particle-wave character. The wave field encodes in its interference structure the past trajectory of the droplet. In the present article we show that this object can self-organize into a spinning state in which the droplet possesses an orbiting motion without any external interaction. The rotation is driven by the wave-mediated attractive interaction of the droplet with its own past. The resulting “memory force” is investigated and characterized experimentally, numerically, and theoretically. Orbiting with a radius of curvature close to half a wavelength is shown to be a memory-induced dynamical attractor for the droplet’s motion.

DOI: [10.1103/PhysRevE.94.042224](https://doi.org/10.1103/PhysRevE.94.042224)

I. INTRODUCTION

Moving wave sources are submitted to a back-reaction resulting from the energy-momentum conservation law. This process is complex when the emission itself depends on the source motion, a general case for isolated sources. The interplay between waves and sources is pivotal in understanding the very nature of elementary particles and their interactions [1,2]. The back-reaction can be considered as a signature of a spatiotemporal nonlocality. This has driven prequantum models of the electron [3–5] and is still present in current field equation theories [2,6,7]. This nonlocality is central in the theory of the recently observed gravitational waves. For these waves on a curved space-time, the back-reaction on the source dynamics is defined by the entire past history of the source [8–11].

Back to earth, about a decade ago, peculiar objects composed of a self-propelled droplet bouncing on a vertically vibrated liquid bath [12–21] have been shown to possess a wave-driven path-memory dynamics [22–24]. The drop can be considered as a pointlike source which is dressed and piloted by the wave field emitted by its previous impacts on the surface. These waves are sustained for a tunable characteristic memory time. For long memory times, the dynamics of these “walkers” becomes complex and bears similarities with quantum particles [25–33]. In particular, in confined geometries, quantized eigenstates emerge resulting from the interplay between the drop trajectory and its associated wave field mode [27–35]. These states were observed in several geometries and interpreted as attractors of the dynamics. In the absence of external force, however, none of these nontrivial attractors had yet been observed.

In the present article, we explore the possible existence of an intrinsic set of such nontrivial attractors. Using this model system, we investigate if the memory-based back-reaction of the wave can produce stable dynamical eigenstates in the absence of any external interactions. In particular, we study the ability to produce self-orbiting states with quantized angular momentum sustained only by a memory force built by the drop past motion. The possibility of such modes was theoretically demonstrated by Oza *et al.* [29]. It was obtained in their investigation of the circular orbits induced by a Coriolis force transverse to the drop motion. They found that in the very long memory limit, orbital states could result only from the wave field in the case of a vanishing Coriolis force. However, these authors concluded that these modes would be intrinsically linearly unstable for all realistic walkers [13,29]. Here we examine experimentally and theoretically another configuration in which such modes can be generated using magnetic walkers gently released from a harmonic potential confinement.

II. PATH-MEMORY-DYNAMICS MODEL

A walker is composed of a droplet bouncing on a vertically vibrated liquid bath and the waves it generates by its successive impacts on the surface. Due to the vertical bath oscillations, the droplet generates at each bounce a localized standing wave packet. The droplet can be seen as a massive pointlike particle propelled and piloted by its self-generated waves sustained by the vertical oscillation [20,22,24]. The resulting global wave field thus contains in its interference structure a memory of the past trajectory of the droplet.

In the vicinity of the Faraday instability, each droplet bounce triggers a quasisustained standing wave that can be approximated by a zero-order Bessel function J_0 with a Faraday wave vector $k_F = 2\pi/\lambda_F$ and $\lambda_F = 4.75$ mm centered at the point of impact [22–24,27]. This building block of the wave field is sustained for a characteristic tunable memory time τ that depends on the relative distance of the vertical acceleration to the Faraday threshold. We can define a nondimensional

*Present address: Matériaux et Phénomènes Quantiques, Université Paris Diderot—CNRS, Sorbonne Paris Cité, 10 rue Alice Domon et Léonie Duquet, 75013 Paris, France.

†Corresponding author: emmanuel.fort@espci.fr

memory parameter $Me = \tau/T_F$ with $T_F = 25$ ms the Faraday period. The wave field $h(\mathbf{r}, t)$ in \mathbf{r} and at time t is thus given by [22,23,27]

$$h(\mathbf{r}, t) = h_0 \sum_{j=-\infty}^0 e^{-\frac{t-t_j}{\tau}} J_0(k_F |\mathbf{r} - \mathbf{r}_j|), \quad (1)$$

where \mathbf{r}_j is the position of the j th past bounce occurring at time t_j and h_0 is the amplitude of a single bounce disturbance. The past trajectory of the droplet is thus encoded within its associated wave field. For this reason, the droplet is said to have a “path-memory dynamics” [22]. The force driving the droplet into motion originates from the wave field asymmetry. At each bounce, the droplet lands on a local slope that gives it a kick.

In the memory range hitherto explored and in the absence of external perturbations walkers are observed to move in a straight line [12,20–24]. However, if set into an initial curved trajectory, one can imagine other possible dynamical solutions due to the persistency of previously generated waves. In the following, we study the characteristics for sustaining, in a circular self-orbiting mode, the walker confined by its own centripetal memory force exerted by the wave field it has emitted during its previous bounces.

III. EXPERIMENTS

The experimental difficulty of testing this idea is that these memory-induced modes require preparing an initial wave field corresponding to a given past trajectory. A “preparation” process is thus needed to force the walker into a trajectory close to that expected for the self-organized mode. The corresponding wave field can therefore be built over time. For this purpose, we first set the drop in rotation on a small orbit by means of an external force and maintain it in this state during a time much longer than the memory time. Only then can the external force be removed to see if the walker keeps orbiting. For this reason we used the experiment in which the walker is submitted to a magnetic central force [31].

To apply a force on the droplet, the oil droplet is loaded with a ferrofluid [31]. By means of two large Helmholtz coils, the whole bath is submitted to a constant vertical magnetic field that polarizes the droplet. In the center of the cell, an additional radial gradient of magnetic field creates a magnetic trap for the drop. This trap was generated by a sharp cone of pure iron that creates a radial gradient by concentrating the magnetic lines of the global field [Fig. 1]. In this setup the magnetic field is entirely produced by the coils. The pure iron has very little hysteresis so that the magnetic field can be entirely removed in less than 1 ms by switching off abruptly the current in the coils. The experimental procedure is the following. The droplet is first magnetically trapped. By tuning the distance between the iron bar and the surface, we choose a situation in which the droplet follows a circular orbit corresponding to the first quantized level of radius of curvature $R_c/\lambda_F \approx 0.37$. The drop is left orbiting for at least 30 s; then the magnetic force is switched off. Figures 2(a) and 2(b) show the evolution of the droplet trajectory when the central force is removed for two values of the memory parameter. At short memory ($Me = 10$) when an abrupt transition is imposed, the drop escapes

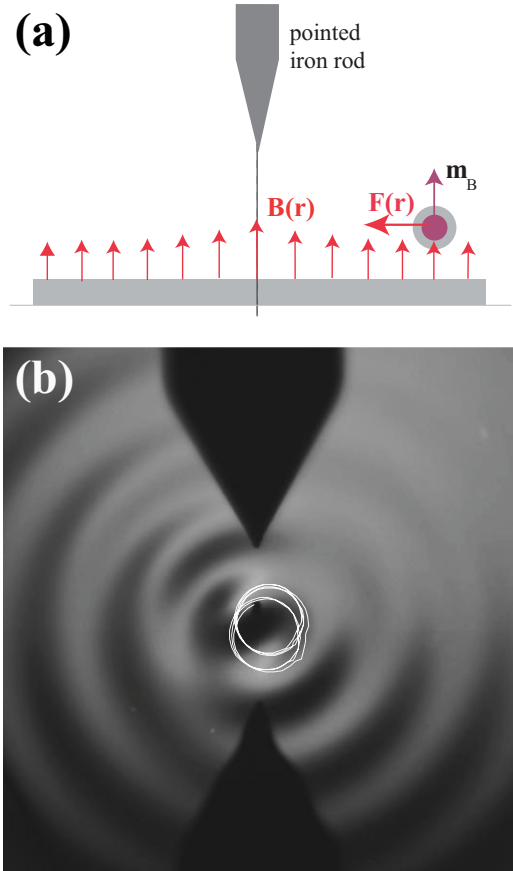


FIG. 1. Experimental realization of self-orbiting modes. (a) Scheme of the core of the experimental setup. The whole bath is submitted to a global magnetic field generated by two coils that are not shown here. A magnetic field maximum is created by the concentration of flux lines due to a sharp rod of pure iron. (b) Top view of the walker in a self-orbiting mode in a long memory regime ($Me \approx 140$). The droplet has a diameter $D \approx 0.7$ mm and a velocity $V \approx 7$ mm s⁻¹. The magnetic field that initially trapped the walker, had been turned off 3 s before this picture was taken. The recent trajectory is superimposed. The nondimensional radius of the free orbit is $R_c/\lambda_F = 0.385 \pm 0.01$.

tangentially almost instantaneously [Figs. 2(a) and 2(c)]. In contrast, at long memory ($Me = 140$) the drop remains trapped in the orbiting motion [Figs. 1(b), 2(b), and 2(d); see Movie S1 in the Supplemental Material [36]]. This effect is optimized when the magnetic field is progressively removed with a characteristic transition time of 1 s.

As shown in Fig. 2(b) the drop keeps orbiting after the complete switch-off. The measurement of the temporal evolution of the orbit radius [Fig. 2(d)] reveals that it undergoes a slight increase at the switch-off. The orbits are then affected by a wobbling motion and the orbital motion survives for a time that ranges from two to six orbital periods after the complete switch-off. This time is up to a few times the memory time τ . Later, a divergence destroys the orbit altogether. These observations show that the self-orbiting modes do exist. In our experimental conditions, however, they become unstable. It is natural to wonder if this is due to an intrinsic instability as predicted in Refs. [13,29] or if, the limited

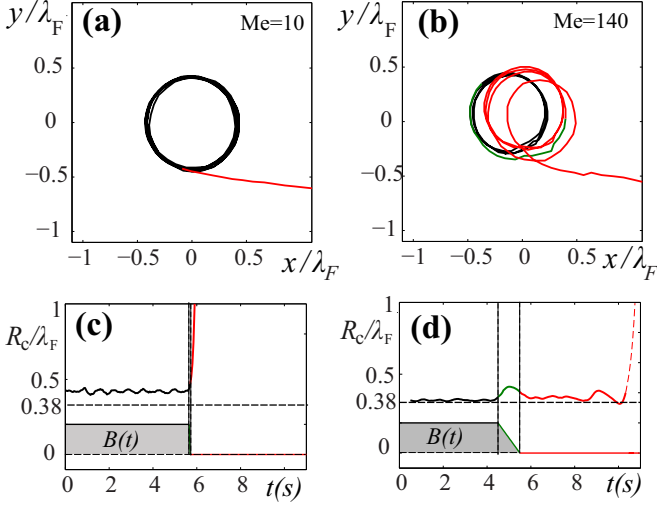


FIG. 2. Typical trajectories observed when the confinement is turned off for two values of the memory parameters. (a) Short memory ($Me \approx 10$). (b) Long memory ($Me \approx 140$) (see Movie S1 [36]). (c,d) Temporal evolution of the normalized trajectory radius R_c/λ_F along these two trajectories (black: magnetic field on, green: transition time, and red: no central force).

lifetime originates from the presence of experimental noise. In the experiment, possible origins for the noise are the presence of wave reflection from the bath walls or ambient air flows. Though difficult to measure, these various noise sources could easily generate variations of a few percent in the wave field amplitudes.

To clarify this point we performed a numerical analysis of existence of the self-orbiting modes and of their stability in the presence of noise.

IV. THE NUMERICAL INVESTIGATION OF THE SELF-ORBITING MODES

We use a discrete iterative model for the walker dynamics reported by our group [22,25,27,31,37] which describes accurately the walker's behavior observed in various experimental situations (the details are given in Ref. [37] and in Appendix A). In this model, both the droplet trajectory and the resulting wave field are computed iteratively. The wave field is given by Eq. (1). The drop motion results from several forces. The wave force, or memory force, is related to the local slope of the interface at the point of bouncing. It is opposed by a tangential frictionlike force F_γ due to both the shearing of the air layer between the droplet and the bath and to the formation of the dip in the interface that will be the source of a new wave. The above-described experiment is simulated by adding an external central force F_m to initially trap the drop. As in the experiment, the force is switched off after some time. Figure 3(a) shows the temporal evolution of the orbital radius for short and long memory, respectively, and insets Figs. 3(b) and 3(c) show the corresponding trajectories after the magnetic force has been switched off. In the long memory regime, the orbiting motion is here (where the noise is weak) stable.

We assess the influence of the noise on the stability of the self-orbiting motion. This Monte Carlo type of analysis has

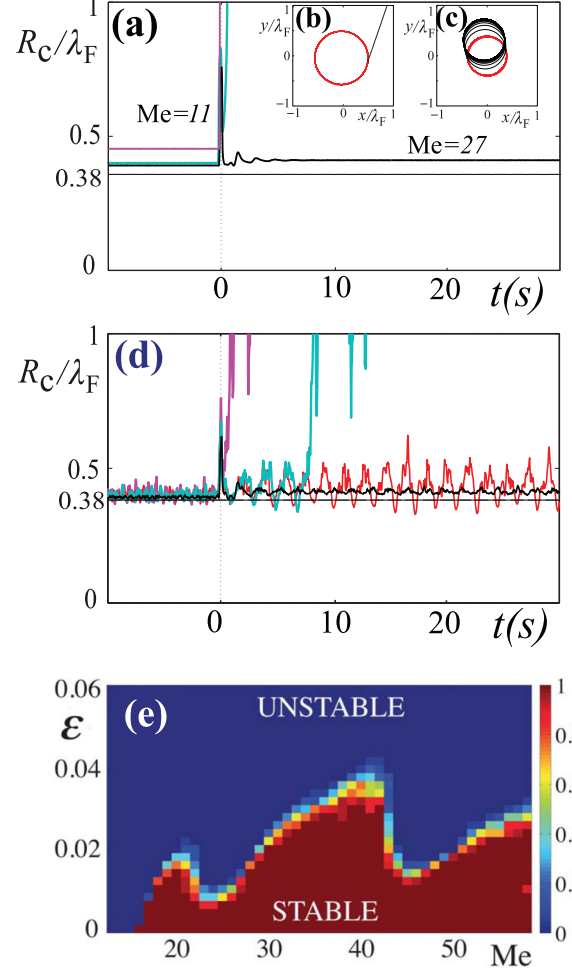


FIG. 3. Numerical investigation of the stability. (a) Temporal evolution of the normalized radius of curvature R_c/λ_F along three trajectories (pink, $Me = 11$; blue, $Me = 15$; black $Me = 27$). The central force is turned off at $t = 0$ s. Insets (b,c) associated trajectories for $Me = 11$, and $Me = 27$. (d) Temporal evolution of the normalized radius of curvature R_c/λ_F for a fixed value of the memory ($Me = 27$) and several values of noise amplitude expressed in radius unit $\varepsilon = \sigma/R$, with R the instantaneous radius: pink, $\varepsilon = 2 \times 10^{-2}$; blue $\varepsilon = 1.6 \times 10^{-2}$; red $\varepsilon = 1.2 \times 10^{-2}$; black $\varepsilon = 4 \times 10^{-3}$. (e) Probability of capture p in the self-orbiting mode (color code on the right) when varying the noise amplitude ε and the memory parameter Me . Each probability is calculated over 20 realizations.

been chosen to account for the nonlinear nature of the walker dynamics. The added noise consists of a random fluctuation of the landing position within an equiprobable disk area of radius $\sigma = \varepsilon R$, with R the orbit radius. Figure 3(d) shows examples of the effect of the added noise on the stability of the released walker for increasing values of ε . The simulation is repeated 20 times for each set of parameters. A probability p of capture in a stable orbit is then computed by measuring the radius after the force switch-off. It is represented as a function of the memory parameter Me and the normalized noise amplitude ε [Fig. 3(e)].

These results permit a general description of the stability of the self-orbiting modes. In the simulations they exist above a critical memory threshold $Me_c = 16$. In the absence of noise [see Fig. 3(a)] the orbit is briefly disturbed by the external

force switch-off and restabilizes after undergoing a brief wobbling motion of decreasing amplitude. In the presence of a noise of moderate amplitude, the wobbling is observed to be sustained without any disruption of the self-orbiting [see Fig. 3(d)]. There is a noise amplitude threshold [depending on the memory, see Fig. 3(e)] above which the wobbling amplification leads to a disruption of the orbital motion. As in the experiment this disruption occurs after a time delay that has a statistically distributed value. The complex dependence with memory of the noise level required to destabilize the initial orbit is beyond the scope of the present article.

V. DISCUSSION AND CONCLUSION

It is interesting to discuss these results in the light of the theoretical work of Oza *et al.* [29]. Their analysis has been triggered by Coriolis experiments with walkers [27,28]. They demonstrate that self-orbits ultimately destabilize. The question is on whether it results from an intrinsic instability of these modes or from noise-induced effects. While our model shows the latter, a linear stability analysis has led Oza *et al.* [29] to conclude to an instability for any realistic walkers.

This limiting case is very difficult to realize experimentally in the case of a force generated by the rotation of the entire bath. Stopping the bath would indeed generate secondary flows both in air and liquid phases. Even in the current magnetic force configuration which is far less disturbing, we find that self-orbits ultimately destabilize. The question is on whether it results from an intrinsic instability of these modes or from noise-induced effects. While our model shows the latter, a linear stability analysis has led Oza *et al.* [29] to conclude to an instability for any realistic walkers.

At least two possible origins of this divergence come to mind. While our model maintains the discrete iterative character of the phenomenon, the MIT model [13] takes a continuous limit. This limit lends itself to a convenient analytical framework. However, it may depart from the particular case of walker dynamics as the bouncing is dominated by discontinuities. In various dynamical systems, it has been shown that the stability of discrete dynamics can strongly differ from their continuous counterpart. As for the stability itself, Oza *et al.* [29] performed a linear stability analysis of these states. However, the walker dynamics is intrinsically nonlinear. This is why we proposed a Monte Carlo approach. Our results show that the self-orbits can be maintained over a long time with or without the presence of wobbling motion. It suggests that even if the orbits were linearly unstable, the nonlinearities play a stabilizing role. This would account for the observed wobbling orbits observed in the simulations. A stability analysis of the circular orbit would consider it unstable while, in a nonlinear perspective, the wobbling does not lead to a bursting of the orbital motion and the angular momentum of the droplet is preserved.

In the orbiting states, the dynamical interplay of the droplet motion and the waves can be best understood by using a decomposition of the wave field reflecting the symmetries of the problem. Using Graf's theorem, it is possible to reformulate the global wave field [given by Eq. (1)] on a basis of Bessel functions centered on the orbit axis of symmetry [31,34,38] (see Appendix B). The radius of the orbit R determines the efficiency of excitation of each eigenmode. Conversely, when evaluated at the droplet position, the contribution of each central Bessel function to the tangential and radial

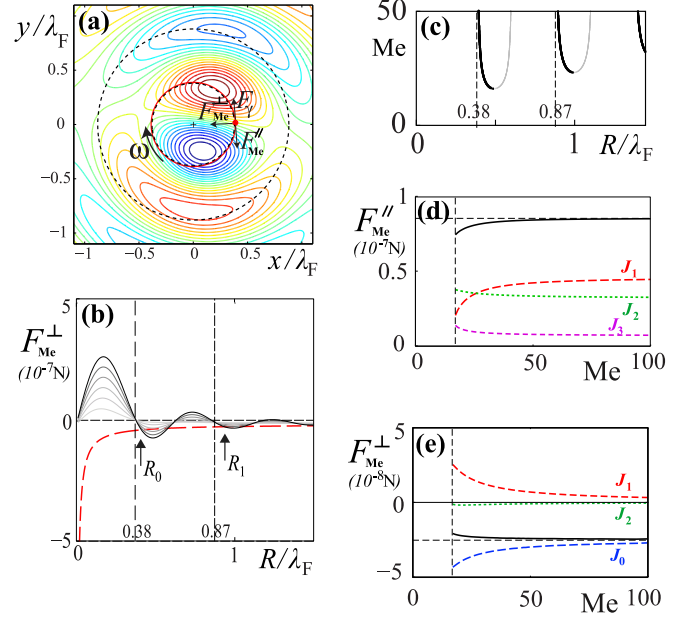


FIG. 4. Theoretical characterization of the forces acting in self-orbits. (a) The computed orbit and wave field at long memory ($Me = 100$). The dotted lines are the zeros of J_0 . (b) The wave-induced radial forces and the centrifugal pseudoforce F_{inert} (dashed red line) as a function of the normalized orbit radius R/λ_F . The estimation wave-induced force is shown for several values of the memory parameters (solid line, from light gray to black: $Me = 11, 15, 19, 23, 27$) with $\frac{Ch_0 k_F}{m_{eff}} = 8.05 \times 10^{-2} N/kg$ and $m_{eff} = 3.82 \times 10^{-7} kg$. Equilibrium is possible when the two curves cross. Vertical lines indicate the first zeros of the J_0 Bessel function R_0 and R_1 . The arrows indicate the stable orbits in the vicinity of R_0 and R_1 . (c) The possible orbits (black lines: stable solutions; gray: unstable solutions) (d) The evolution with memory of the contributions of the first Bessel modes to the tangential force $F_{Me}^{//}$ with an equilibrium speed $V = 10.9$ mm/s which enables to estimate $\gamma = 7.8 \times 10^{-6} kg/s$. (e) The evolution with memory of the contributions of the first Bessel modes to the radial force F_{Me}^{\perp} . The dashed lines represent the contribution of the first three centered Bessel modes. The vertical line indicates the critical memory parameter Me_c ; the horizontal line shows the asymptotic value of $F_{Me}^{\perp} = F_{inert}$ when $J_0(k_F R) = 0$.

forces can be obtained (see Appendix B). It is convenient to analyze the drop dynamics by decomposing the memory force $\mathbf{F}_{Me} = -C[\nabla h]_{r(r)}$ into its tangential $F_{Me}^{//}$ and radial F_{Me}^{\perp} components [see Fig. 4(a)], with C the wave coupling constant. For the self-orbiting mode to exist, the self-propulsion of the walker must be maintained for increasing Me . Velocity results from the balance between $F_{Me}^{//}$ and a friction force $F_{\gamma} = -\gamma V$: $V = 1/\gamma F_{Me}^{//}$. Both $C \times h_0$ and γ are constants that we estimate from the experiments [21,22]. Their values are in accordance with those predicted by the hydrodynamic analysis done by Moláček and Bush [19,24].

We compute the equilibrium radius from Eq. (1) for the radius measured experimentally. This latter is close to the first zero of the J_0 Bessel mode R_0 (as will be discussed below). Figure 4(d) shows the variations of $F_{Me}^{//}$ as a function of the memory parameter Me . In addition, the contribution of each central Bessel function to $F_{Me}^{//}$ can be evaluated

using Graf's theorem calculated at the droplet position. F_{Me}^{\perp} is nearly constant above Me_c . At long memory, it takes the limiting value of $\frac{2Ch_0}{T_F} \sum_{n>0} J_n^2(k_F R_0)/(R_0 \omega)$ (see the Appendix B). Apart from the axisymmetric J_0 Bessel mode, all the Bessel modes could contribute to the local tangential slope. However, when evaluated near the first zero of the J_0 Bessel mode only Bessel functions of order $n = 1$ and 2 have significant contributions to the tangential propulsion (representing, respectively, approximately 52% and 38% of the tangential slope). These modes rotate at the angular frequency ω of the droplet maintaining a constant local slope at the point of impact, resulting in a sustained propulsion, as observed experimentally. In other terms such a structure is intrinsically endowed with an "arrow of time". When their two-dimensional (2D) trajectory is circular, the space-time symmetry is helical.

We can now examine the situation in the radial direction. The droplet rotating on an orbit of radius R is submitted to the memory-induced force F_{Me}^{\perp} . This latter satisfies $F_{\text{Me}}^{\perp} = -C\partial h/\partial r|_{r=R}$ and can be computed directly from Eq. (1). Figure 4(b) shows F_{Me}^{\perp} for different memory parameters Me as a function of the normalized radius of the orbit R/λ_F (see Appendix B). The inertial pseudoforce $F_{\text{inert}} = -m_{\text{eff}} V^2/R$ is also plotted with the constant droplet velocity approximation. The radial balance can only be reached for a discrete set of radii for which $F_{\text{inert}} = F_{\text{Me}}^{\perp}$ above a critical memory parameter $\text{Me}_c \approx 16$. The number of crossings, associated to larger radii, increases with increasing memory. The solutions in Fig. 4(b) for which the slope of the memory force is positive at the crossing are trivially nonstable. For the others, the radii of the self-orbits decrease towards the zeros of the J_0 Bessel functions (dotted vertical lines) as the memory increases [Fig. 4(c)]. In the following, we will focus on the smallest orbit observed experimentally associated with the first zero of the J_0 Bessel function, i.e., with $R/\lambda_F = R_c/\lambda_F = 0.38 \pm 0.01$.

We can understand this evolution using the decomposition in centered Bessel modes. Figure 4(e) shows the memory-induced force F_{Me}^{\perp} as a function of Me together with the contributions of centered Bessel modes $n = 0, 1$, and 2. With increasing memory, the role of the central J_0 Bessel function is the leading contribution of the wave field to the radial force. At long memory ($\text{Me} \gg \text{Me}_c$), the radial force takes the simple expression

$$F_{\text{Me}}^{\perp} \simeq Ch_0 k_F \text{Me} J_0(k_F R) J_1(k_F R). \quad (2)$$

F_{Me}^{\perp} is the product of three terms: $J_1(k_F R)$ arises from the radial derivative at $k_F R$ of the J_0 mode, $J_0(k_F R)$ is the J_0 mode excitation amplitude by the droplet bounces at a radius R , and Me is the number of bounces that contributes to the global wave field [22]. We can now understand why the radii R/λ_F of the self-orbiting modes tend to the zeros of the J_0 Bessel function as Me increases [see Figs. 4(b) and 4(c)]. It results from a self-organized mechanical balance. Since F_{inert} does not depend on the memory parameter, the product $\text{Me} J_0(k_F R)$ has to remain constant to maintain the force balance $F_{\text{inert}} = F_{\text{Me}}^{\perp}$. Hence, at critical memory parameter Me_c , the walker maximizes the contribution of each bounce to reach a sufficient wave force to balance inertia. This becomes possible above Me_c and with a radius that is at a maximum of $J_0(k_F R)$. As memory increases, the number of bounces that contributes

to the wave force increases; their individual contributions to the global wave field must decrease. In the long memory limit, each individual contribution tends to zero. The self-orbit radius then satisfies

$$\frac{R}{R_0} \approx 1 + \frac{\beta}{\text{Me}} \quad \text{with} \quad \beta = \frac{m_{\text{eff}}}{Ch_0} \left[\frac{V}{k_F R_0 J_1(k_F R_0)} \right]^2, \quad (3)$$

where $k_F R_0$ is a zero of the J_0 Bessel function. Equations (2) and (3) are similar to those found in Oza *et al.* [29]. This fine-tuning balancing the centrifugal inertial force can be interpreted as a spatiotemporal self-organization of the walker. This self-orbiting mode is an attractor of the dynamical system.

The previous analysis takes the point of view of the particle: The wave field is only considered through its interaction with the droplet only and not *per se*. For instance, the added angular momentum brought by the wave field to the droplet is the result of a local coupling and is thus different from the angular momentum of the whole wave field. We now discuss the global features of the wave field, its energy E_{wave} , and angular momentum L_{wave} .

As the wave is monochromatic, the energy stored in the wave field E_{wave} is proportional to the square of the surface displacement $h(\mathbf{r}, t)$ integrated over the surface of the bath (see Appendix C). This energy is normalized by the wave field energy induced by a single bounce modeled as a J_0 Bessel function. Figure 5(a) shows the dependence of the normalized energy E_{wave} stored in the wave field as a function of the memory parameter Me for a self-orbiting mode and for a droplet moving in a straight line.

While E_{wave} increases with memory for the rectilinear motion, it slowly decreases for the self-orbiting mode, reaching a finite value in the high memory limit. However, the wave energy resulting from a single bounce does not depend on the considered trajectory: Each impact generates a wave modeled by a J_0 Bessel function of equal amplitude. Since all the individual bounces produce coherent waves, each wave source interferes constructively or destructively depending on their relative position. The contribution of each new source to the energy of the global wave field can thus be either positive or negative. Hence, the energy of the global wave field holds a wave information of the droplet's past trajectory. It is the wavelike signature of the droplet path.

Since centered Bessel functions form an orthogonal basis, it is possible to decompose the dimensionless wave field energy on these Bessel modes:

$$E_{\text{wave}} = \sum_{n \geq 0} E_{\text{wave}, n}, \quad (4)$$

where $E_{\text{wave}, n}$ is the energy of the J_n centered Bessel function normalized by the energy of a J_0 Bessel function corresponding to a single bounce. Figure 5(a) shows the contributions of Bessel modes of order $n = 0, 1$, and 2 to the global wave field energy. Only these first three modes contribute significantly to the wave field energy. The energy of the centered J_0 is given by $E_{\text{wave}, 0} = \text{Me}^2 J_0^2(k_F R)$ (see Appendix C). At first sight, this energy could diverge with memory. However, as mentioned previously, this mode is responsible for the radial force balance of the droplet [see Fig. 4(c)]. Hence, the radius of the self-orbit undergoes a self-tuning to maintain $E_{\text{wave}, 0}$ constant. As a result, with increasing memory, $k_F R$ tends to a zero of the J_0

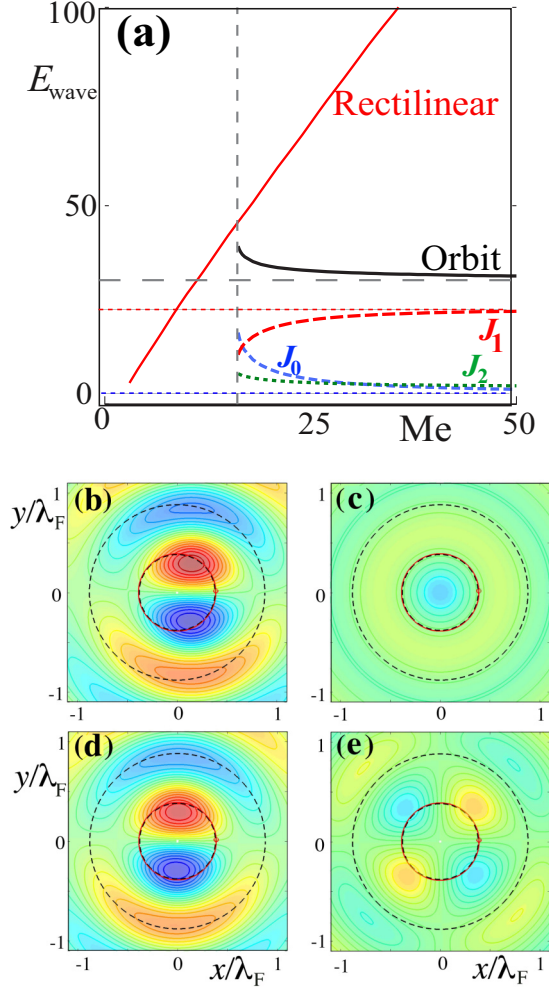


FIG. 5. Energy stored in the global wave field and its modes. (a) The evolution of the global wave field energy of a walker with the memory. While it diverges for a free walker walking linearly (in red), it reaches a finite value for a self-orbiting mode (black line). The contribution of the first three centered Bessel modes are shown in dashed lines. The vertical line indicates the critical memory parameter Me_c . The horizontal line indicates the energy of the self-orbit mode for long memory. (b) The surface profile at approximately the time of impact of the droplet with the surface. The colors distinguish the protrusions in red from the troughs in blue. (c,d,e) show the contributions to the surface height of the first three centered Bessel wave modes J_0 , J_1 , and J_2 , respectively. The radius of the orbit (black line) is slightly larger than that of the first nodal line of J_0 (dashed black line). As shown in Fig. 4 the centripetal force exerted on the drop is essentially due to J_0 while the tangential force is due to J_1 and J_2 .

Bessel function [see Eq. (3)]. This self-organization leads to a memory independent finite limit at long memory satisfying $E_{\text{wave},0} \simeq (k_F R_0 \beta)^2 J_1^2(k_F R_0)$. The energy of the other modes only depends marginally on the memory parameter. At long memory, $E_{\text{wave},n>0} \simeq 2J_n^2(k_F R_0)/(n\omega T_F)^2$. When evaluated in $k_F R_0$, the amplitude of the Bessel functions tends rapidly to 0 with increasing n . Hence, only modes $n = 1$ and 2 contribute significantly to the wave field energy. The variations of the contribution between the different modes just above Me_c

originate in the evolution of the self-orbiting radius towards R_0 . Figures 5(b)–5(e) show the wave field associated to the self-orbiting mode in the long memory limit together with its decomposition in centered Bessel modes. In agreement with the energy analysis, the J_1 Bessel mode is dominant. Note that, in the infinite memory limit, the amplitudes of all the nonzero Bessel functions are fixed. In contrast, J_0 being to oppose inertia, its amplitude depends on droplet mass.

The projection onto the Bessel mode orthonormal basis enables a calculation of the angular momentum of the wave field since $L_{\text{wave}} = \sum_{n>0} L_{\text{wave},n}$ where $L_{\text{wave},n}$ is the angular momentum of the centered J_n Bessel function. For an angular frequency ω , $L_{\text{wave},n} = \frac{nE_{\text{wave},n}}{\omega}$ [39]. As discussed before [Fig. 5(a)], in the case of self-orbiting modes, the energy contributions of all the nonzero Bessel modes rapidly reach a finite limit at long memory. Hence, the normalized angular momentum of the wave field also tends to a finite value. The symmetries of the trajectory are present in the wave field. The trajectory being spatiotemporally helical, it possesses an intrinsic angular momentum. As memory increases, the contributions of all the bounces along the trajectory for one revolution become more alike. Consequently, the axial asymmetry along the droplet path decreases on the scale of one turn. However, when integrated over the memory time, a constant asymmetry is recovered. The constant velocity of the droplet is a direct consequence of the helical symmetry of its trajectory. Note that similar angular momentum exchanges have been observed in optical tweezers using Bessel beams. The orbital angular momentum of the light beam sets trapped microparticles into rotation [40]. In the case of walkers, contrary to standard static external potentials that are limited to spatial symmetries, the dynamical potential associated with the wave field holds the whole spatiotemporal symmetry of the trajectory.

The self-orbiting mode is surprising, in particular because the rotation center does not coincide with the center of mass. As shown above, this is a direct consequence of the role of the wave field. It is interesting to compare this motion with the more standard situation in which two identical droplets orbit symmetrically around their center of mass. This binary motion has already been studied [12,21,37] and it was shown that the orbits could only have discrete sizes. For in-phase bouncing droplets, the discrete set of possible radii is also related to the successive zeros of the J_0 Bessel function. However, in this latter case the orbiting results from a mutual attraction: It exists even at short memory, being due to the effect on each drop of the wave emitted by the other.

For self-orbiting modes, the effect of the memory secondary sources in the radial direction is similar to that of a virtual drop that would be bouncing with the same phase and diametrically opposed to the real one [27]. A self-orbit is thus in a sense a binary spinning system composed of a massive pointlike object (the droplet) set in rotation by its interaction with a virtual counterpart. This mirror droplet is the echo of the past trajectory brought to the present by the wave field. This spatiotemporal nonlocal dynamics of the walkers makes possible the rotation around a center different from the center of mass. It is tantalizing to attribute an effective mass to the wave field to recover the rotation around the center of mass for a walker. In the case of short-memory limit already, the walker

behaves as if it was slightly heavier [13,27,29,31,41,42], but in the case of self-rotating states, the wavelike counterpart of the droplet should then be endowed with an identical mass, similar to a twin droplet rotating system. The effective angular momentum of the self-orbiting droplet should then be doubled when compared with that of an undressed droplet. It is interesting to note that a charged self-orbiting droplet would in this case possess a half-integer gyromagnetic ratio that cannot be found when mass and charge have a similar spatial distribution.

We have shown that self-orbits are attractors for free walkers. Thus it is natural to wonder if more generally these attractors play a role in nonisolated dynamics at long memory. Figure 6(a) shows the trajectory of a droplet in a wide potential (defined by $\Lambda \approx 2$; see [35]) at very high values of the memory (e.g., $Me \geq 500$). The motion is then highly chaotic (intermittence) and in frequent occurrence the droplet is observed to be trapped in orbiting motion. It performs one or several successive orbits before escaping and getting trapped in another self-orbit motion elsewhere. The observation of the waves [Fig. 6(b)] reveals that the local structure of the wave field is then very similar to that observed in self-orbits [see Fig. 1(b)]. These small scale orbits are statistically relevant; if the radius of curvature R_S is measured along the whole trajectory a peak is observed centered at a value $R_S = 0.37\lambda_F$. The presence of these elementary orbits, each endowed with a fixed elementary unit of angular momentum, appears to be general. It is also observed at very high memory for other types of confinement, when the walker is enclosed in corrals, for instance [Fig. 6(c)]. These small orbits are the first building blocks of complex trajectories observed at high values of the memory parameter ($Me > 100$) in confined geometries. In previous articles investigating the walker dynamics in an attractive potential, it was shown that the dynamics of walkers could be analyzed in terms of time scales [34]. While the short time scale effect is simply responsible for the walker's propulsion, the intermediate scale can generate spontaneously pivotal structures around which the droplet performs U turns. At a larger time scale, these pivots can become the building blocks of a self-organization into a global coherent orbital motion [34]. However, this is only possible in very narrow ranges of values of the width of the confining potential well. In all other cases the pivots cannot become coherently spatially organized in a global mode and the resulting frustration results in chaotic motion [35]. At long memory, the dynamics of a confined walker is essentially determined by a self-organization between the droplet motion and its wave field. This is why the signature of self-orbiting attractors emerges systematically.

ACKNOWLEDGMENTS

We are grateful to Jean Claude Bacri, Florence Gazeau, Sophie Neveu, Jacques Servais, and Claire Wilhem for their help in creating this experimental setup. We are grateful to Vincent Bacot, Christian Borghesi, Antonin Eddi, Marc Miskin, and Julien Moukhtar for fruitful discussions. The authors acknowledge the support of the AXA research fund and the French National Research Agency (Grants No. ANR-10-LABX-24 and No. ANR-10-IDEX-0001-02-PSL*).

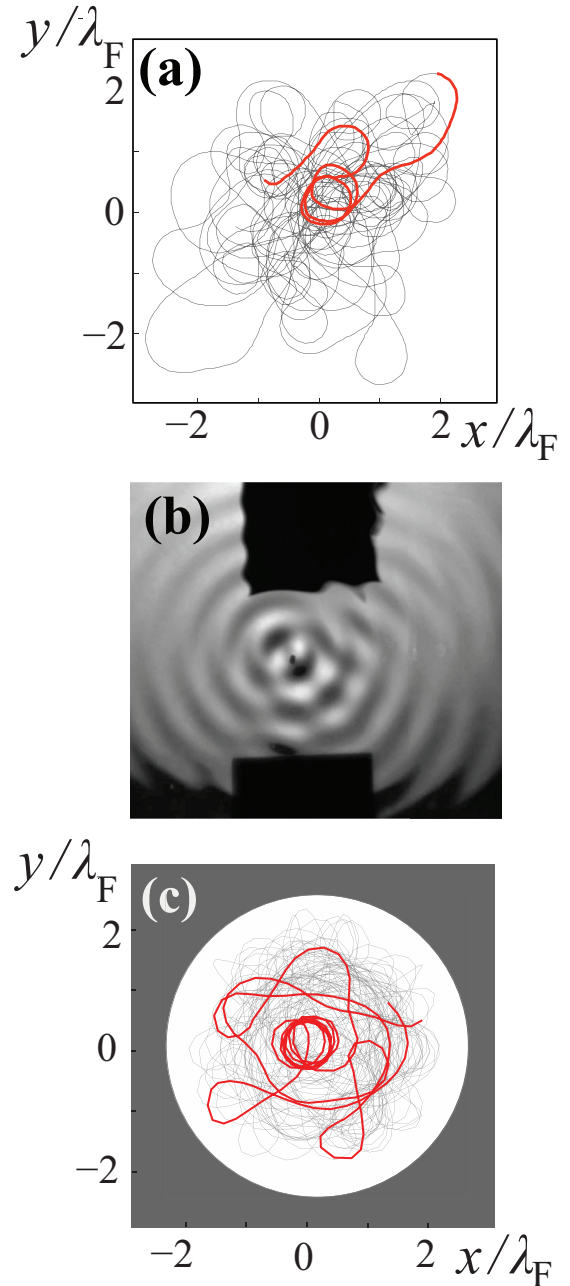


FIG. 6. Spontaneous transient self-orbiting loops. At very long memory, the trajectory of a confined walker exhibits generically the spontaneous formation of multiple transient self-orbiting loops. (a) Trajectory in a wide potential well at $Me = 500$. (b) Photograph of the wave field structure in this regime showing, in the vicinity of the drop, the self-organized structure of a small self-orbit. (c) The same transient self-orbits observed when a long memory walker is confined in a circular corral.

APPENDIX A: PATH-MEMORY MODEL

We consider a vibrated bath of silicon oil with an acceleration amplitude γ_m typically between $4.2g$ and $4.5g$ (the Faraday threshold γ_F is at $4.5g$). In the latter range, a submillimetric drop is bouncing in the period-doubling regime

and is self-propelled. The horizontal dynamics is decoupled from the vertical one.

1. Vertical dynamics

We restrict ourselves to the period-doubling regime: two oscillations of the bath per drop bounce. The position of the bath is denoted $z_b = z_{b,0} \sin \omega_0 t$ with $\omega_0 = 2 \times 2\pi/T_F$ and $T_F = 25$ ms the Faraday period. The vertical dynamics is sequentially decomposed as follows.

The drop takes off for the first time at t_0 when the gravity is balanced by the bath acceleration. Once t_0 determined, the following takeoffs occur sequentially at times $\{t_0 + nT_F\}_{n \in \mathbb{N}}$. The drop takes off with an initial vertical speed $v_{z,0} = \omega_0 z_{b,0} \cos \omega_0 t_0$ and an altitude $z_0 = z_{b,0} \sin \omega_0 t_0$. Once in the air, the vertical dynamics of the drops is dictated by the equation $\ddot{z}_b = -g$ with the initial conditions given above.

The landing time t_l corresponds to the time at which the drop altitude matches the bath surface again. The time spent in the air is denoted $\Delta t_{\text{air}} = t_l - t_0$ while the contact time is given by $\Delta t_{\text{surf.}} = T_F - \Delta t_{\text{air}}$.

Experimentally, the bath oscillates at a frequency of 80 Hz and at an amplitude $z_{b,0} \approx 1.8 \times 10^{-4}$ m. Thus, the bath acceleration is about $4.3g$. With these parameters, the initial take-off phase is at $\omega_0 t_0 = 0.21$, $\Delta t_{\text{air}} = 19.5$ ms $= 0.78 T_F$, and $\Delta t_{\text{surf.}} = 5.5$ ms $= 0.22 T_F$. These numerical value are in accordance with those of Moláček and Bush [24].

2. Horizontal dynamics

The drop is modeled as a point. When the drop is in the air, we numerically solve the horizontal equation of motion with a Runge-Kutta method (ODE45, with MATLAB).

The speed just before the n th landing is noted \mathbf{v} and can be decomposed into a term \mathbf{v}_{\parallel} tangential to the surface and one \mathbf{v}_{\perp} perpendicular. The transfer of horizontal momentum depends on the angle between the incoming speed and the normal of the surface \mathbf{n} . If the surface field h is of small amplitude compared to the Faraday wavelength, the relation between the horizontal speed just before $\mathbf{v}_{\parallel}(t_n^-)$ and the speed just after $\mathbf{v}_{\parallel}(t_n^+)$, at the n th landing, is given by $\mathbf{v}_{\parallel}(t_n^+) - \mathbf{v}_{\parallel}(t_n^-) = -|\mathbf{v}_{\perp}| \nabla_{\parallel} h$.

During the “contact” time, the drop loses a part of its energy due to its interaction with the bath which leads to $v_{\parallel}(t_n^+ + \Delta t_{\text{surf.}}) = v_{\parallel}(t_n^+) e^{-\Delta t_{\text{surf.}}/T_v}$. The characteristic time is $T_v = 5$ ms which means that $v_{\parallel}(t_n^- + \Delta t_{\text{surf.}})/v_{\parallel}(t_n^+) \approx 0.35$. Note that the total horizontal restitution coefficient $C_{\parallel} = v_{\parallel}(t_n^+ + \Delta t_{\text{surf.}})/v_{\parallel}(t_n^-)$ is about twice as large. This agrees with the measurements of Moláček and Bush [24] who give an approximate value of $\approx 0.7 \pm 0.1$ in the Weber regime of interest.

3. Field evolution

The surface field seen by the drop at the phase of impact ϕ is updated at each bounce. At the n th landing, the surface field is $h(\mathbf{r}, t_n^-)$ [see Eq. (1)].

The gradient of the surface field is taken at the drop position. The remaining coefficient h_0 is chosen so that the walking speed matches the experimental one (10 mm/s) in the case $F_{\text{ext.}} = 0$ and at high memory. The field is initialized as $h(\mathbf{r}, t = 0) = 0$. Note that this numerical model contains no

free parameter [22]. Only the memory Me and/or the external forces are control parameters.

APPENDIX B: COMPUTATION OF THE FORCE EXERTED BY THE WAVE FIELD

This force is due to the bouncing of the drop on a locally slanted surface and is proportional to the local slope. In order to obtain this force we first compute the global wave field $h(\mathbf{r}, t)$ and expand it on the wave basis of centered Bessel modes $\{J_n(k_F r) e^{in\theta}\}_{n \in \mathbb{Z}}$. It gives

$$h(\mathbf{r}, t) = h_0 \sum_{j=-\infty}^0 e^{-\frac{t-t_j}{\tau}} \sum_{n=-\infty}^{+\infty} J_n(k_F r) J_n(k_F r_j) e^{-in(\theta-\theta_j)}. \quad (\text{B1})$$

In the case of a circular motion, with a radius R and an angular velocity ω , without loss of generality we choose at the time of impact t , the angular position of the drop ωt .

We have the following for all j : $r_j = R$, $t - t_j = jT_F$, and $\theta_j = \omega t - \omega jT_F$, where θ_0 is the angular position of the drop at $t = t_0$, an arbitrary constant which depends on the choice of the frame axis. It gives

$$h(\mathbf{r}, t) = \frac{h_0}{T_F} \sum_{n=0}^{+\infty} (2 - \delta_{n,0}) J_n(k_F R) J_n(k_F r) \tau \times \left\{ \frac{\cos[n(\theta - \omega t)]}{1 + (n\omega\tau)^2} - \frac{n\omega\tau \sin[n(\theta - \omega t)]}{1 + (n\omega\tau)^2} \right\}, \quad (\text{B2})$$

with $\delta_{n,0}$ the Kronecker symbol.

For the radial force we get

$$F_{\text{Me}}^{\perp} = Ch_0 k_F \frac{\tau}{T_F} J_0(k_F R) J_1(k_F R) - \frac{1}{\tau} \left\{ C \frac{h_0 k_F}{T_F} \sum_{n=0}^{+\infty} J_n(k_F R) [J_{n-1}(k_F R) - J_{n+1}(k_F R)] \times \left[\frac{\tau^2}{1 + (n\omega\tau)^2} \right] \right\}. \quad (\text{B3})$$

In the long memory limit $\omega\tau \gg 1$, we have the simplification

$$F_{\text{Me}}^{\perp} = Ch_0 k_F \text{Me} J_0(k_F R) J_1(k_F R) + O\left(\frac{1}{\text{Me}}\right), \quad (\text{B4})$$

with $\text{Me} = \frac{\tau}{T_F}$ which justifies Eq. (2) in the long memory limit. For the tangential force, we get

$$F_{\text{Me}}^{\parallel} = \frac{2C}{V} \frac{h_0}{T_F} \sum_{n=1}^{+\infty} J_n^2(k_F R) \left[\frac{(\omega n\tau)^2}{1 + (n\omega\tau)^2} \right], \quad (\text{B5})$$

with $V = \omega R$. In the high memory limit $\omega\tau \gg 1$, the force can be expressed as

$$F_{\text{Me}}^{\parallel} = \frac{2C}{V} \frac{h_0}{T_F} \sum_{n=1}^{+\infty} J_n^2(k_F R) = \frac{C}{V} \frac{h_0}{T_F} [1 - J_0^2(k_F R)]. \quad (\text{B6})$$

APPENDIX C: COMPUTATION OF THE WAVE FIELD ENERGY

Let us evaluate the energy stored in the wave field E_{wave} normalized by the wave field energy induced by a single bounce modeled as a J_0 Bessel function.

The energy of the wave field for a monochromatic wave over a domain Ω of radius \mathcal{R} is proportional to the square of the surface displacement $h(\mathbf{r}, t)$ integrated over the surface of the bath. Using the wave basis of the centered Bessel functions $\{J_n(k_F r)e^{in\theta}\}_{n \in \mathbb{Z}}$, the energy can thus be written as

$$E \propto h_0^2 \sum_{n=-\infty}^{+\infty} A_n^2 \iint_{\Omega} J_n^2(k_F r) d^2 \mathbf{r}. \quad (\text{C1})$$

In the case of a walker orbiting at a radius R with an angular velocity ω , from Eq. (7) we obtain $A_n^2 = \frac{1}{T_F^2} J_n^2(k_F R) \frac{\tau^2}{1+(n\omega\tau)^2}$. Normalizing the wave energy in the domain Ω by that of a single bounce E_{bounce} gives

$$E_{\text{wave}} = \lim_{\mathcal{R} \rightarrow \infty} \frac{E}{E_{\text{bounce}}} \simeq \sum_{n=-\infty}^{+\infty} A_n^2. \quad (\text{C2})$$

It is possible to write $E_{\text{wave}} = \sum_{n \geq 0} E_{\text{wave}, n}$ by defining $E_{\text{wave}, n}$ as the energy of the J_n centered Bessel function normalized by the energy of a J_0 centered Bessel mode corresponding to a single bounce. In particular, $E_{\text{wave}, 0} = \text{Me}^2 J_0^2(k_F R)$.

-
- [1] N. Bohr, *Philos. Mag.* **26**, 1 (1913).
 - [2] P. A. M. Dirac, *Proc. R. Soc. London, Ser. A* **167**, 148 (1938).
 - [3] M. Abraham, *Ann. Phys.* **10**, 105 (1903).
 - [4] M. Abraham, *Phys. Z.* **5**, 576 (1904).
 - [5] H. A. Lorentz, *The Theory of Electrons* (Teubner, Leipzig, 1916; Dover, New York, 1952).
 - [6] J. P. Dowling, *Electron Theory and Quantum Electrodynamics: 100 Years Later* (Plenum, New York, 1997).
 - [7] M. Springford, *Electron: A Centenary Volume* (Cambridge University Press, Cambridge, 1997).
 - [8] L. Blanchet and T. Damour, *Phys. Rev. D* **37**, 1410 (1988).
 - [9] L. Blanchet and T. Damour, *Phys. Rev. D* **46**, 4304 (1992).
 - [10] L. Blanchet, *Living Rev. Relativity* **5**, 3 (2002).
 - [11] B. P. Abbott *et al.*, *Phys. Rev. Lett.* **116**, 061102 (2016).
 - [12] Y. Couder, S. Protiere, E. Fort, and A. Boudaoud, *Nature* **437**, 208 (2005).
 - [13] J. W. M. Bush, *Ann. Rev. Fluid Mech.* **47**, 269 (2015).
 - [14] M. Hubert, F. Ludewig, S. Dorbolo, and N. Vandewalle, *Physica D* **272**, 1 (2014).
 - [15] T. Gilet, N. Vandewalle, and S. Dorbolo, *Phys. Rev. E* **76**, 035302 (2007).
 - [16] N. Vandewalle, D. Terwagne, K. Mulleners, T. Gilet, and S. Dorbolo, *Phys. Fluids* **18**, 091106 (2006).
 - [17] D. Terwagne, N. Vandewalle, and S. Dorbolo, *Phys. Rev. E* **76**, 056311 (2007).
 - [18] A. Eddi, A. Boudaoud, and Y. Couder, *Europhys. Lett.* **94**, 20004 (2011).
 - [19] J. Moláček and J. W. M. Bush, *J. Fluid Mech.* **727**, 582 (2013).
 - [20] P. A. Milewski, C. A. Galeano-Rios, A. Nachbin, and J. W. M. Bush, *J. Fluid Mech.* **778**, 361 (2015).
 - [21] S. Protiere, A. Boudaoud, and Y. Couder, *J. Fluid Mech.* **554**, 85 (2006).
 - [22] A. Eddi, E. Sultan, J. Moukhtar, E. Fort, M. Rossi, and Y. Couder, *J. Fluid Mech.* **674**, 433 (2011).
 - [23] A. U. Oza, R. R. Rosales, and J. W. M. Bush, *J. Fluid Mech.* **737**, 552 (2013).
 - [24] J. Moláček and J. W. M. Bush, *J. Fluid Mech.* **727**, 612 (2013).
 - [25] Y. Couder and E. Fort, *Phys. Rev. Lett.* **97**, 154101 (2006).
 - [26] A. Eddi, J. Moukhtar, S. Perrard, E. Fort, and Y. Couder, *Phys. Rev. Lett.* **108**, 264503 (2012).
 - [27] E. Fort, A. Eddi, A. Boudaoud, J. Moukhtar, and Y. Couder, *Proc. Natl. Acad. Sci. USA* **107**, 17515 (2010).
 - [28] D. M. Harris and J. W. M. Bush, *J. Fluid Mech.* **739**, 444 (2014).
 - [29] A. Oza, D. M. Harris, R. R. Rosales, and J. W. M. Bush, *J. Fluid Mech.* **744**, 404 (2014).
 - [30] A. U. Oza, Ø. Wind-Willassen, D. M. Harris, R. R. Rosales, and J. W. M. Bush, *Phys. Fluids*, **26**, 082101 (2014).
 - [31] S. Perrard, M. Labousse, M. Miskin, E. Fort, and Y. Couder, *Nat. Commun.* **5**, 3219 (2014).
 - [32] D. M. Harris, J. Moukhtar, E. Fort, Y. Couder, and J. W. M. Bush, *Phys. Rev. E* **88**, 011001 (2013).
 - [33] T. Gilet, *Phys. Rev. E* **90**, 052917 (2014).
 - [34] M. Labousse, S. Perrard, Y. Couder, and E. Fort, *New J. Phys.* **16**, 113027 (2014).
 - [35] S. Perrard, M. Labousse, E. Fort, and Y. Couder, *Phys. Rev. Lett.* **113**, 104101 (2014).
 - [36] See Supplemental Material at <http://link.aps.org/supplemental/10.1103/PhysRevE.94.042224> for a stroboscopic film showing the orbital motion of a droplet in a circular orbit of radius $R \approx 0.37\lambda_F$. The dark part of each image is the pure iron pointed rod on which is attached a small lamp: when it is lit the magnetic field is on. At approximately half the film length the current (and the lamp) are switched off and the droplet is observed to keep orbiting. The memory parameter equals $\text{Me} = 140$.
 - [37] C. Borghesi, J. Moukhtar, M. Labousse, A. Eddi, E. Fort, and Y. Couder, *Phys. Rev. E* **90**, 063017 (2014).
 - [38] E. Fort and Y. Couder, *Europhys. Lett.* **102**, 16005 (2013).
 - [39] P. H. Ceperley, *Am. J. Phys.* **60**, 938 (1992).
 - [40] K. Volke-Sepulveda, V. Garcés-Chávez, S. Chávez-Cerda, J. Arlt, and K. Dholakia, *J. Opt. B* **4**, S82 (2002).
 - [41] M. Labousse, A. U. Oza, S. Perrard, and J. W. M. Bush, *Phys. Rev. E* **93**, 033122 (2016).
 - [42] J. W. M. Bush, A. U. Oza, and J. Moláček, *J. Fluid Mech.* **755**, R7 (2014).